

Two families of elliptical plasma lenses

Xinzhong Er¹  Adam Rogers² 

¹ *South-Western Institute for Astronomy Research, Yunnan University, Kunming, P.R.China*

² *Department of Physics and Astronomy, Brandon University, Brandon, MB, R7A 6A9, Canada*

26 July 2019

ABSTRACT

Plasma lensing is the refraction of low-frequency electromagnetic rays due to free electrons in the interstellar medium. Although the phenomenon has a distinct similarity to gravitational lensing, particularly in its mathematical description, plasma lensing introduces other additional features, such as wavelength dependence, radial rather than tangential image distortions, and strong demagnification of background sources. Axisymmetrical models of plasma lenses have been well-studied in the literature, but density distributions with more complicated shapes can provide new and exotic image configurations and increase the richness of the magnification properties. As a first step towards non-axisymmetrical distributions, we study two families of elliptical plasma lens, softened power-law and exponential plasma distributions. We perform numerical studies on each lens model, and present them over a parameter space. In addition to deriving elliptical plasma lens formulae, we also investigate the number of critical curves that the lens can produce by studying the lens parameter space, in particular the dependence on the lensing ellipticity. We find that the introduction of ellipticity into the plasma distribution can enhance the lensing effects as well as the complexity of the magnification map.

Key words: gravitational lensing: strong - gravitational lensing: micro, Interstellar medium

1 INTRODUCTION

Compact radio sources exhibit intervals of rapid change in their flux-density, which have been attributed to extreme scattering events (ESEs). The first ESEs were discovered decades ago (Fiedler et al. 1987), but the construction of detailed physical models to describe all aspects of the phenomenon remains open. The millisecond duration pulses known as fast radio bursts (FRBs; Lorimer et al. 2007; Pen 2018; Cordes & Chatterjee 2019), may also be related to plasma lensing in a dense medium, though it remains unknown if this environment is located in the host galaxy, or is an intervening structure along the line of sight. The chromaticity of FRBs suggests that strong refraction by plasma structures in the intervening interstellar medium (ISM) may be related to the origin of these events. Additionally it has been observed that the 2-dimensional dynamic power spectra of some pulsars contain remarkably organized parabolic structures (e.g. Stinebring et al. 2001; Stinebring 2007), which can be explained by highly-anisotropic diffractive scattering of radio waves from the pulsar (e.g. Walker et al. 2004; Cordes et al. 2006). Moreover, the radio pulsar time delay has been attributed to plasma structures in the ISM (e.g. Shannon & Cordes 2017). Plasma distributions en-

closing compact objects have also been shown to alter their appearance (Rogers 2017).

Refractive plasma lens models have been developed that describe plasma density distributions analytically. As the prototypical example, Clegg et al. (1998) studied the properties of a one dimensional Gaussian plasma lens. This model has been widely applied through the literature and forms the basis for analytical models of isolated plasma distributions (e.g. Dong et al. 2018). It has been suggested that the plasma lensing in the host galaxies of FRBs can modulate the amplitudes of the bursts (Cordes et al. 2017). This analysis was undertaken using a one-dimensional Gaussian lens. In addition, Vedantham et al. (2017a,b); Kerr et al. (2018) present the case of an ESE with typical U-shaped and W-shaped light curves, which was modelled using a superposition of two one-dimensional Gaussians to build up a dual-lobed morphology for a slice across the plasma density. The small scale magnetic field in the black widow pulsar system PSR B1957+20 has been revealed due to lensing in which plasma stripped from the pulsar’s companion acts to magnify the pulsar during eclipses (Li et al. 2018; Suresh & Cordes 2018). Coles et al. (2015) models the Astronomical Unit (AU) scale plasma lensing for pulsar observations, and also suggests an electron density on the order of $\sim 10 \text{ cm}^{-3}$. In addition, model independent inversion methods have also been developed and applied to data directly. The dynamic spectrum of the ESE in the radio loud quasar PKS 1939-315 was used to determine the column density

* xer@ynu.edu.cn

† RogersA@BrandonU.CA

profile of the plasma lens (see, for example, [Bannister et al. 2016](#); [Tuntsov et al. 2016](#)).

Despite these successes, there are lingering mysteries that remain regarding the nature of plasma lensing. It is difficult to interpret the high density and pressures within isolated plasma lenses. The dispersion measure (DM), i.e. the integrated column density of free electrons between the observer and the source, necessary to account for the lensing effect is too large ($\sim 10^3 \text{ cm}^{-3}$) for a structure in the ionized interstellar medium ([Clegg et al. 1998](#)), and cannot exist in pressure balance with the ambient interstellar medium in the Milky Way (e.g. [Cordes & Lazio 2002](#)). Some suggestions have been put forth, e.g., it requires modest electron density if highly elongated plasma sheets are seen from an edge-on perspective ([Romani et al. 1987](#); [Goldreich & Sridhar 2006](#); [Pen & Levin 2014](#); [Simard & Pen 2018](#); [Briskin et al. 2010](#)). The plasma sheet has also been found in numerical simulations of the supernova-driven turbulence (e.g. [Hill et al. 2012](#)). On the other hand, previous studies on plasma lens models mainly focus on the axis-symmetrical Gaussian distribution of the electrons, which is a smooth density profile. However, there is the more realistic possibility of asymmetry and clumpiness in the electron density. The ellipticity and small scale variations of the lens may increase the lensing efficiency, e.g. the lens with low electron density may also generate high magnifications. Moreover, the distribution of the ionized interstellar medium may be affected by the stellar wind or the explosion of the supernovae, and forms a highly elongated shape. Thus, the investigation of different density profiles, especially the elliptical models is required. In particular, the shape of shock fronts can be approximated by the highly elliptical models and explicit analytical models can help us.

[Bannister et al. \(2016\)](#) have demonstrated the usefulness of real-time, multi-wavelength monitoring of ESEs in progress. Their work provides a new ESE detection method, which formed the basis for the Australia Telescope ESE project (ATESE; [Bannister et al. 2016](#); [Tuntsov et al. 2017](#)) that is positioned to detect many more such events in progress and map the column density through the lenses with dedicated monitoring. Such observations have been used to eliminate the possibility of an isotropic spherical lens structure, favoring anisotropic projected densities instead, such as shells and filaments. However, this does not mean that all such ESEs are formed by lenses with the same morphologies. In fact, the spherical Gaussian lens ([Clegg et al. 1998](#)) remains the most widely applied lens model to date in the ESE literature and remains relevant today ([Cordes et al. 2017](#)). It is well within the possibility that the distinction between an elliptical and spherical lens could be feasible by an analogous observational campaign. More monitoring of ESEs in progress is required.

The “non-parametric” ESE modeling performed by [Tuntsov et al. \(2016\)](#) shows that more observations are required to distinguish between axisymmetric and highly anisotropic lenses. The elliptical lens is a versatile model that interpolates between spherical and highly anisotropic charge distributions. Thus, elliptical lenses naturally bridge two extremes that represent the most successful and interesting options for modeling ESEs.

The deflection by the plasma on a given frequency is similar in practice to gravitational lensing. Thus, well-established theory in gravitational lensing (e.g. [Schneider et al. 1992](#); [Perlick 2000](#)) can be adopted for studying plasma lensing, although there is some difference in the plasma lens case. First of all, gravitational lensing mainly occurs on cosmological scales (e.g. [Schrabback et al. 2010](#)), caused by massive objects such as galaxies (e.g. [Koopmans et al. 2009](#)) or galaxy clusters (e.g. [Clowe et al. 2006](#)). The exception is

microlensing by stars within the Galaxy (e.g. [Mao 2012](#)). In reality, the microlensing case is similar to the plasma lensing, since in both scenarios the deflection occurs on small scales and depends on the relative motion between the lens and the source. Mass models for gravitational lenses are well studied from galaxy dynamics (e.g. [Binney & Tremaine 1987](#); [Czoske et al. 2012](#); [Barnabè et al. 2012](#); [Li et al. 2019](#)) and cosmological simulations (e.g. [Navarro et al. 1997](#); [Schaller et al. 2015](#); [Xu et al. 2016](#)). In contrast, for plasma lenses, only simple symmetrical models for the electron density have been largely considered. Model degeneracy has been found between symmetric dual-component plasma lens distributions and an asymmetric model used to fit the ESE in PKS 1939-315 ([Tuntsov et al. 2016](#); [Rogers & Er 2019](#)). The parametric model shows that this distribution is one of a larger family in which two lenses act on a source.

In general, plasma lenses are diverging, however they can cause large magnifications if they are offset from the background source along the observers line of sight. It thus will enrich the variability of the light curves, e.g. a volcano shape in the pulsar light curves (e.g. [Coles et al. 2015](#)). Moreover, the deflection due to the plasma lens is chromatic. Only in the radio bands can significant signatures be observed. In extremely low frequency observations, ray optics may no longer apply and wave effects may become significant. Wave asymptotes in plasma lensing have also been studied recently ([Grillo & Cordes 2018](#)).

In current observations, the frequency ranges mainly from a few MHz to a few GHz (e.g. [Briskin et al. 2010](#); [Coles et al. 2015](#)). Therefore, wave effects may not strong enough to be detected (e.g. [Nakamura & Deguchi 1999](#); [Nambu 2013](#)). Even in geometric optics, the optical properties of plasma lens models need to be systematically studied for magnification and critical curves ([Cordes & Lazio 2002](#)). For example, the Gaussian or axisymmetric profiles have been discussed by [Scalo & Elmegreen \(e.g. 2004\)](#). In this work, we will follow similar methodology of geometric optics as in gravitational lensing to study the magnification and critical curves in plasma lensing. We study two families of analytical models for the electron distribution. In particular, we focus on the ellipticity of the plasma density, and how it will increase the magnification. Elliptical models of gravitational lenses have been widely studied both analytically and numerically (e.g. [Keeton 2001](#)). In gravitational lensing, it has been shown that the elliptical distribution and the small scale variations, i.e. substructures can significantly changed the lensing properties, such as increase the cross section of the multiple images. The elliptical gravitational lenses show high efficiency of generating multiple images and high magnification. Two kinds of elliptical models have been studied in the gravitational lens literature, which introduce ellipticity into the lens potential (e.g. [Blandford & Kochanek 1987](#); [Schrann 1990](#)) or by means of an elliptical mass density (e.g. [Kassiola & Kovner 1993](#); [Kormann et al. 1994](#); [Keeton & Kochanek 1998](#); [Tessore & Metcalf 2015](#)). Unlike in gravitational lensing, the plasma effective lensing “potential” is proportional to the projected density of electrons. The ellipticity in the potential and electron density will give the same result. Thus, we will modify the lens potential into an elliptical form in this work. We present the elliptical exponential plasma lenses and softened power-law (SPL) lenses and discuss the properties of the magnification in Section 3. We summarize our conclusions in Section 4. A gallery of criticals and caustics for a selection of elliptical lens examples is shown in the appendix.

In our study we will consider pulsars or AGN, which will be treated as point sources in our calculations. Another approximation

is the effect of cosmological distances (e.g. the difference between angular diameter distance and luminosity distance) will not taken into account as we assume that the lenses are within our Galaxy.

2 BASIC FORMULAE

We will outline the basic formulae regarding the two families of plasma lenses in this work. More details can be found in [Er & Rogers \(2018\)](#). The notation follows the general gravitational lens formalism discussed in [Schneider et al. \(1992\)](#); [Narayan & Bartelmann \(1996\)](#). For astrophysically relevant situations, the lens is considered weak. Due to the large distances between the source and lens (D_{ds}) and the distances from lens and source to the observer (D_d and D_s respectively) compared to the diameter of the lens structure, the thin lens approximation can be adopted (see e.g. [Narayan & Bartelmann 1996](#)). We introduce angular coordinates $\theta = \sqrt{\theta_1^2 + \theta_2^2}$ with respect to the line-of-sight, and those on the source plane as β . They are related through the lens equation

$$\beta = \theta - \alpha = \theta - \nabla_\theta \psi(\theta), \quad (1)$$

where α is the deflection angle, ψ is the effective lens potential and ∇_θ is the gradient on the image plane.

2.1 Exponential Lenses

The exponential lenses are a widely used model to describe ESEs, since the Gaussian lens model introduced by [Clegg et al. \(1998\)](#) to model observations of the extragalactic sources 0954+654 and 1741-038 is a special case of the exponential model. We follow the description of exponential models in [Er & Rogers \(2018\)](#) and the Gaussian lens in [Clegg et al. \(1998\)](#), and specify the projected electron distribution on the lens plane $N_e(\theta)$. This choice is made to compare with the most common parameterization in the literature ([Clegg et al. 1998](#)). We adopt a form for the electron column density in the lens plane,

$$N_e(\theta) = N_0 \exp\left(-\frac{\theta^h}{h\sigma^h}\right) \quad (\theta > 0), \quad (2)$$

with N_0 the maximum electron column density within the lens and σ as the width of the lens for $h > 0$ ([Vedantham et al. 2017a](#); [Er & Rogers 2018](#)). The projected electron density gives the potential

$$\psi(\theta) = \theta_0^2 \exp\left(-\frac{\theta^h}{h\sigma^h}\right) \quad (3)$$

and deflection angle

$$\alpha_{\text{exp}}(\theta) = -\theta_0^2 \frac{\theta^{(h-1)}}{\sigma^h} \exp\left(-\frac{\theta^h}{h\sigma^h}\right) \quad (4)$$

with the characteristic angular scale

$$\theta_0 = \lambda \left(\frac{D_{\text{ds}}}{D_s D_d} \frac{1}{2\pi} r_e N_0 \right)^{\frac{1}{2}}, \quad (5)$$

where λ is the observing wavelength and r_e is the classical electron radius. The wavelength of a photon λ can vary in the gravitational field via the gravitational redshift effect, which introduces an additional complication to the deflection angle. Since we are only discussing lensing from plasma, the gravitational deflection will not be taken into account in this work.

For each h value, we can define a critical limit below which the

exponential lenses produce no critical curves, and therefore only a single image: $\theta_0 < f(h)\sigma$, and

$$f(h) = \left[F^{\frac{h-2}{h}} (F + 1 - h) e^{\frac{-F}{h}} \right]^{-1/2}, \quad (6)$$

where the factor F is

$$F = \frac{1}{2} \left[3(h-1) + \sqrt{(h-1)(5h-1)} \right]. \quad (7)$$

One can find more detail about the critical limit in [Er & Rogers \(2018\)](#); [Rogers & Er \(2019\)](#).

2.2 Power-Law Lenses

The optical properties of the power-law (PL) lens are determined by the charge volume density $n_e(r)$ (Sec. 2.2.1). The general approach to setting up the lensing equations is to project the volume density to the lens plane to produce $N_e(\theta)$, the column density. Therefore, with a model for the charge volume density n_e we can find the column density and derive the lens potential, deflection angle and magnification. However, rather than putting the ellipticity directly into the volume density n_e , we can instead parameterize the 2D projection, the column-density $N_e(\theta)$ (the dispersion measure (DM) of the lens; Sec. 2.2.2). This approach of parameterizing the projected electron density follows [Clegg et al. \(1998\)](#), who originally used it to establish the successful Gaussian lens. However, as we will show, the two approaches produce power-law lens models that are simple transformations of one another. This behaviour is radically different from the two related elliptical gravitational lens models, one of which includes ellipticity in the potential ([Kassiola & Kovner 1993](#)) and the other includes ellipticity in the mass distribution ([Keeton & Kochanek 1998](#)). Let us investigate both cases below.

2.2.1 Volume-Density Power-Law

The family of power-law lenses is produced by a three-dimensional electron volume density given by

$$n_e(r) = n_0 \frac{R_0^h}{r^h} \quad (8)$$

with the power-law index h and the characteristic radius R_0 at which $n_e(R_0) = n_0$. This electron density profile produces an effective lens potential ([Er & Rogers 2018](#)):

$$\psi(\theta) = \begin{cases} -\theta_0^2 \ln \theta, & h = 1 \\ \frac{\theta_0^{h+1}}{(h-1)\theta^{h-1}}, & h \neq 1 \end{cases} \quad (9)$$

The lens potential gives the deflection angle

$$\alpha_{\text{PL}}(\theta) = -\frac{\theta_0^{h+1}}{\theta^h} \quad (10)$$

which is written in terms of the characteristic angular scale

$$\theta_0 = \left(\lambda^2 \frac{D_{\text{ds}}}{D_s D_d} \frac{r_e n_0 R_0^h}{\sqrt{\pi}} \frac{\Gamma\left(\frac{h}{2} + \frac{1}{2}\right)}{\Gamma\left(\frac{h}{2}\right)} \right)^{\frac{1}{h+1}}. \quad (11)$$

The deflection angle for this density distribution was first evaluated by [Muhleman & Johnston \(1966\)](#), and [Bisnovatyi-Kogan & Tsupko \(2009\)](#) present a study from gravitational lensing by a compact object embedded in a non-uniform plasma.

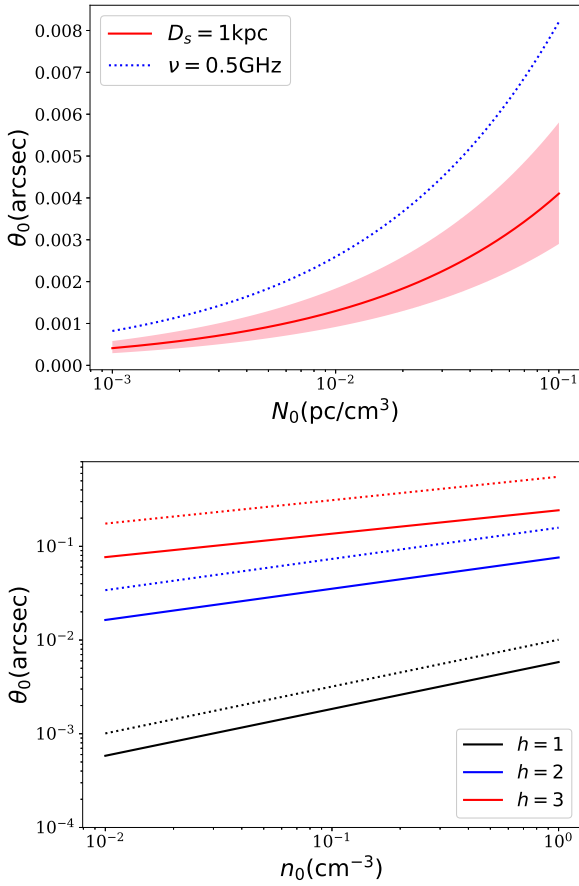


Figure 1. The characteristic angular scale θ_0 as a function of electron density for circular plasma lens models. Top panel shows the exponential models: the red solid (blue dotted) line presents the relation for $\nu = 1$ GHz (0.5GHz) with source distance $D_s = 10$ kpc. The lens is placed at the mid-point between the source and the observer. The shaded area denotes a variety of source distances between 5 and 20 kpc. The bottom panel shows the power-law models with different power index h . The solid (dotted) lines present results of $R_0 = 0.1(0.3)$ pc.

In order to soften the singularity at the origin, it is trivial to include a finite core θ_c by simply making the transformation $\theta \rightarrow \sqrt{\theta^2 + \theta_c^2}$ in the deflection angle. Similar to the exponential lens, we derive a critical value of the core size required to produce a critical curve. This limit is given in terms of the characteristic angular scale, such that

$$\theta_{\text{crit}} = \theta_0 \left[2 \left(\frac{3}{h} + 1 \right)^{-\frac{h+3}{2}} \right]^{\frac{1}{h+1}}. \quad (12)$$

For $\theta_c > \theta_{\text{crit}}$, the power-law lens cannot form critical curve. The detail about the core size can be found in [Rogers & Er \(2019\)](#).

The characteristic angular radius θ_0 indicates the lens strength for the circularly symmetric lens. We thus show θ_0 as a function of electron density for the two families of models in Fig. 1. In the exponential model (top panel), θ_0 depends on the density and distance. We can see that the projected electron density increases by two order of magnitudes, but θ_0 only increases by a factor of about 8. A similar dependence can be seen in the power-law models (bottom panel): the electron density does not have a large impact on the lens strength θ_0 . On the other hand, the power index can dra-

matically change the lens strength for the power-law lens, e.g. θ_0 in model with $h = 3$ (red lines) is about 200 times larger than that of $h = 1$ (black lines). Therefore, we need to consider the density profile as well in the plasma, e.g. radial gradient and ellipticity rather than only the maximum density itself. As we will present in the following, the lens ellipticity can improve the lens strength as well as the richness of magnification properties. For simplicity, we will use arcsec for the unit in the following discussion if not mentioned.

2.2.2 Column-Density Power-Law

Now let us consider the family of power-law lenses given by a two-dimensional electron column density that has a power-law form

$$N_e(\theta) = N_0 \frac{\theta_R^H}{\theta^H}, \quad (13)$$

with the power-law index H and the angular radius θ_R at which $N_e(\theta_R) = N_0$. This electron column density produces an effective lens potential

$$\psi(\theta) = \frac{\lambda^2}{2\pi} \frac{D_{ds}}{D_d D_s} r_e N_0 \theta_R^H \frac{1}{\theta^H} \quad (14)$$

Notice here that $\psi(\theta) \propto 1/\theta^H$ whereas the volume-density case has a deflection angle with this dependence instead. Following the usual approach, the gradient of the potential gives

$$\alpha = -\frac{\theta_0^{H+2}}{\theta^{H+1}}, \quad (15)$$

where we have defined

$$\theta_0 = \left(\frac{\lambda^2}{2\pi} \frac{D_{ds}}{D_d D_s} r_e H N_0 \theta_R^H \right)^{\frac{1}{H+2}}. \quad (16)$$

The deflection angle differs from the volume density PL lens result by an extra factor of θ_0/θ . θ_0 can have the same definition if we use the substitutions below. This gives distinct behaviour for the magnification,

$$\mu^{-1} = 1 - H \frac{\theta_0^{H+2}}{\theta^{H+2}} - (H+1) \frac{\theta_0^{2(H+2)}}{\theta^{2(H+2)}}. \quad (17)$$

Note that this is quadratic in $\theta_0^{H+2}/\theta^{H+2}$, so we can easily find the critical curves of this lens using the quadratic formula,

$$\frac{\theta_0}{\theta_{\text{crit}}} = \left(-\frac{H \pm (H+2)}{2(H+1)} \right)^{\frac{1}{H+2}} \quad (18)$$

We can discard the additive solution in the above expression, which will not produce any real solutions for any value of H . This means the negative case produces an overall positive quantity which gives real solutions in the root. The remaining solution produces

$$\theta_{\text{crit}} = \theta_0 [H+1]^{\frac{1}{H+2}}. \quad (19)$$

These equations are identical to the deflection angle and magnification for the volume-density lens provided that we make the substitution $H+1 \rightarrow h$. The lensing potential and characteristic angular scale can be reproduced provided we make the substitutions $R_0/D_d \rightarrow \theta_R$ and

$$N_0 \rightarrow 2 \frac{n_0 R_0}{(h-1)} \sqrt{\pi} \frac{\Gamma(\frac{h}{2} + \frac{1}{2})}{\Gamma(\frac{h}{2})}. \quad (20)$$

Since the lensing magnification and image formation properties of this charge column-density lens are effectively identical to the charge volume-density lens, we will restrict the remainder of our analysis to the volume-density lens case.

3 ELLIPTICAL PLASMA LENSING MODELS

We generalize the lens models of previous section by introducing an elliptical coordinate $\Theta = \sqrt{\theta_1^2 q + \theta_2^2/q}$, where q is the axis ratio (Kassiola & Kovner 1993; Kormann et al. 1994). The ellipticity of the density distribution can be given by $\epsilon = (1-q)/(1+q)$. The value of the axis ratio q is only taken from the interval $0 < q \leq 1$, as it is equivalent for θ_1 - and θ_2 -axis. Thus in the following calculations, $q < 1$ is assumed, and the circularly symmetric model is obtained in the limiting case $q \rightarrow 1$. We only consider the iso-elliptical distribution, i.e. the ellipticity is the same for each radius.

3.1 Exponential model

For the exponential models, the elliptical potential can be obtained by substituting Θ for θ in Eq. 3. The deflection angle is

$$\alpha = -2A(h) (\theta_1 q + i\theta_2/q), \quad (21)$$

where the pre-factor is given by

$$A(h) = \frac{\theta_0^2 \Theta^{h-2}}{2\sigma^h} \exp\left(-\frac{\Theta^h}{h\sigma^h}\right). \quad (22)$$

The lensing convergence and shear are

$$\begin{aligned} \kappa &= A(h) \left[-q - 1/q - \left(\frac{(h-2)}{\Theta^2} - \frac{\Theta^{h-2}}{\sigma^h} \right) (\theta_1^2 q^2 + \theta_2^2/q^2) \right], \\ \gamma &= A(h) \left[-q + 1/q - \left(\frac{(h-2)}{\Theta^2} - \frac{\Theta^{h-2}}{\sigma^h} \right) (\theta_1^2 q^2 - \theta_2^2/q^2) \right. \\ &\quad \left. + 2i \left(\frac{\Theta^{h-2} \theta_1 \theta_2}{\sigma^h} - (h-2) \frac{\theta_1 \theta_2}{\Theta^2} \right) \right]. \end{aligned} \quad (23)$$

We use complex notation for the two shear components. The imaginary part represents the second component of the shear (Kormann et al. 1994).

The lens magnification is defined as the Jacobian determinant of the thin lens equation. This can be stated in terms of the convergence,

$$\mu^{-1} = 1 - 2\kappa + \frac{\partial \alpha_1}{\partial \theta_1} \frac{\partial \alpha_2}{\partial \theta_2} - \frac{\partial \alpha_1}{\partial \theta_2} \frac{\partial \alpha_2}{\partial \theta_1}. \quad (24)$$

Using this expression we derive the elliptical exponential lens magnification for general h ,

$$\begin{aligned} \mu^{-1} &= 1 - 2A(h) \left[-q - \frac{1}{q} + \left(\frac{\theta_1^2 q^2 + \theta_2^2/q^2}{\Theta^2} \right) \left(2 - h + \frac{\Theta^h}{\sigma^h} \right) \right] \\ &\quad + 4A^2(h) \left(h - 1 - \frac{\Theta^h}{\sigma^h} \right). \end{aligned} \quad (25)$$

For $h = 2$, the expression becomes an elliptical Gaussian lens, and the magnification can be written as

$$\mu^{-1} = 1 - 2A(2) \left(-q - \frac{1}{q} + \frac{\theta_1^2 q^2 + \theta_2^2/q^2}{\sigma^2} \right) + 4A(2)^2 \left[1 - \frac{\Theta^2}{\sigma^2} \right] \quad (26)$$

One can obtain the maximum demagnification of Gaussian lens at the origin

$$\mu_{\text{origin}} \leq \frac{1}{(1 + (\theta_0/\sigma)^2)^2}. \quad (27)$$

In the circular limit, the demagnification is the strongest at the origin. The ellipticity further increases the demagnification, which can

vary based on the trajectory of the source behind the lens. Moreover, the frequency dependence of μ_{origin} can provide further constraints on the model parameters. For lenses with $h < 2$ the magnification at the origin vanishes and the lens has an exclusion region. For lenses with $h > 2$, the magnification at the origin approaches unity, producing a W-shaped light curve, as opposed to a U-type light curve consistent with the result derived in Er & Rogers (2018) for symmetric exponential lenses and equivalent to Rogers & Er (2019) for a binary lens.

We first show the Young diagram of exponential models for $h = 1, 2, 3$ in Fig. 2. The blue, red and black line represents the super-, critical and sub-critical case in the circular lens models respectively (Er & Rogers 2018). The solid line shows the source position as a function of the image plane position along the major (θ_1 -) axis, while the dotted line shows the same plot except along the minor (θ_2 -) axis. As we can see that the deflection along the major axis is mild and without rapid variation, and the deflection along the minor axis shows rapid change even for the sub-critical cases. We therefore expect strong changes in magnification along the minor axis, even for the sub-critical lens.

In Fig. 3, two dimensional magnification maps on the lens plane are shown for $h = 1, 2, 3$ respectively. The green colour stands for the positive magnification, with pink for the negative. The solid (dotted) blue lines show the critical curves (caustics). The red and yellow curves indicate the boundary of $\mu = +1$ and $\mu = -1$ on the lens plane (solid lines) and on the source plane (dotted lines) respectively. In the light colour regions, the images will be demagnified. The lens with $h = 1$ has a dumbbell shape critical, while the lenses of $h = 2, 3$ have two separated kidney-like arcs. The demagnification region of $h = 1$ extended along the major axis, while that of $h = 2, 3$ are mainly concentrated near the lens origin. With different trajectories of the background source, the elliptical lenses can produce a rich series of magnification curves, and those along the minor axis are similar to that produced by the circular lens. In the right panel of Fig. 3, there is a light green region at the origin, where the magnification is close to unity. It has been observed that such a spike can cause model degeneracy (Rogers & Er 2019). A corresponding magnification map on the source plane is shown in Fig. 4. We focus on the center region of the lens as this map is computationally expensive. There is a large, extended exclusion region around the center of the lens. Along the minor axis, there is a sharp boundary, while along the major axis, the variations are smooth. One can extract the magnification curve given a trajectory of the background source. Those near the minor axis are similar to that generated by a spherical lens.

In the appendix, a set of criticals and caustics are displayed selected from the lens parameter space. Some of them show similar shapes to dual-component plasma lenses (Rogers & Er 2019).

The critical curves provide useful properties of the lensing. They indicate strong variations in the magnification map, corresponding to spikes on the light curve of a background source. The critical curve also sections the lens plane into regions that count the number of multiple images. Moreover, the number of critical curves in plasma lensing tightly correlates with the density profile of the electron in axisymmetric lens (Er & Rogers 2018), such as the ratio between θ_0 and σ in exponential models. In order to characterize the behavior of the elliptical lens, we explore the parameter space of the lens model as a function of q and θ_0 . For each (q, θ_0) pair, we calculate the determinant of the Jacobian metric on a finite coordinate grid (θ_1, θ_2) and contour the determinant to reveal the curves over which it vanishes. This set of curves are the lens criticals. We then count the number of contours that a given (q, θ_0) pair

provides. The parameter space map is shown in Fig. 5. From top to bottom, we show lenses with $h = 1, 2, 3$ respectively. In general, the lens families of higher index h are more efficient in generating critical curves. For $h = 1$, the lenses generate one critical in most cases, although the shape of criticals can vary dramatically (see appendix). Two criticals can be generated when the two parts of a dumbbell demagnification region break apart from one another. In the parameter space, these situations only occur within a small area (blue region). For $h = 2, 3$, the lenses generate two symmetric criticals on both side of the major axis. The two arc-shape criticals shrink and degrade to the two ellipses and eventually approach the circular lens case with the increasing of q .

We also present the lens with an extremely high ellipticity ($q = 0.05$), which is different from the ellipticity of galaxy or dark matter halo (e.g. Allgood et al. 2006; Schrabback et al. 2015). The ellipticity significantly increases the lensing efficiency. The elongated lens with sub-critical θ_0 (much smaller than the critical value) can also generate critical curves, as we show in Fig. 6. For such a plasma lens, the required central density N_0 to have critical curves will be one order smaller than that of a circular lens.

3.2 Power-law model

We further generalize the power-law model to the elliptical softened power-law (ESPL) model. The lens potential can be generalized from Eq. 9 by making the substitution $\theta \rightarrow \Theta = \sqrt{\theta_1^2 q + \theta_2^2 / q + \theta_c^2}$. The deflection angle given by the ESPL lens is

$$\alpha(\theta) = -\frac{\theta_0^{h+1}}{\Theta^{h+1}} (\theta_1 q + i\theta_2 / q), \quad (28)$$

and the lensing convergence and shear

$$\kappa = -B(h) \left[q + 1/q - (h+1) \frac{\theta_1^2 q^2 + \theta_2^2 / q^2}{\Theta^2} \right]; \quad (29)$$

$$\gamma = -B(h) \left[q - 1/q - (h+1) \frac{\theta_1^2 q^2 - \theta_2^2 / q^2}{\Theta^2} - i \frac{2(h+1)\theta_1\theta_2}{\Theta^2} \right], \quad (30)$$

where pre-factor $B(h) = \theta_0^{h+1} / (2\Theta^{h+1})$. The inverse magnification can be written as

$$\mu^{-1} = 1 + 2B(h) \left[q + 1/q - (h+1) \frac{\theta_1^2 q^2 + \theta_2^2 / q^2}{\Theta^2} \right] - 4hB(h)^2 + 4(h+1)B(h)^2 \frac{\theta_c^2}{\Theta^2}, \quad (31)$$

The demagnification at the lens origin has an upper limit as well

$$\mu_{\text{origin}} \leq \frac{1}{\left(1 + \frac{\theta_0^{h+1}}{\theta_c^{h+1}}\right)^2}. \quad (32)$$

It depends on the ratio between the core radius θ_c and θ_0 , and a large core radius weakens the lensing effects and provides a potential explanation for the observations with weak demagnification. The ellipticity however will increase the lensing demagnification. We further simplify the mathematics by considering the singular case, i.e. $\theta_c = 0$, and regress the magnification to one dimension on the θ_1 - and θ_2 -axis. The critical curve crosses the two axis at

$$\theta_{1c} = \theta_0 \left(\frac{h}{q^{(h-1)/2}} \right)^{\frac{1}{h+1}}, \quad \theta_{2c} = \theta_0 \left(h q^{(h-1)/2} \right)^{\frac{1}{h+1}}. \quad (33)$$

For the softened model, the existence of the critical curve depends

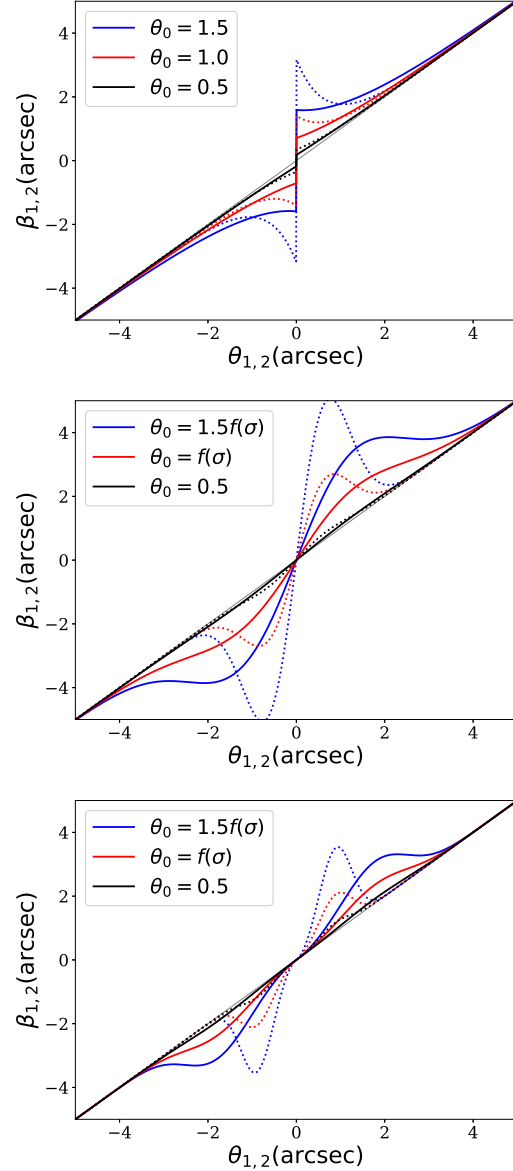


Figure 2. The Young diagram of the exponential models with $\sigma = 1.0$, $q = 0.5$. Grey line indicates the identity. From top to bottom, we present the exponential lenses with $h = 1, 2, 3$ respectively. The solid (dotted) lines indicate the mapping along the major (minor) axis of the lens. The formula of critical condition $f(\sigma)$ can be found in Er & Rogers (2018).

on θ_c and can be solved numerically. For the lenses of $h = 1$, the critical curve cross both two axis at the same length without dependence on the axis ratio q , i.e. $\theta_{1c} = \theta_{2c} = \theta_0$.

In Fig. 7, the Young diagram of ESPL lenses with axis ratio $q = 0.5$ is shown. The same colour code is applied here: the blue, red and black lines represent the super-, critical and sub-critical case in the circular lens models respectively. The solid and dotted line shows the source position as a function of the image plane position along the major and minor axes, respectively. Similar as in the one-dimensional case, increasing the core size weakens the lensing effects but causes more complicated lensing behaviour, which can be seen from the number of criticals. The deflection angles along the major axis are slightly smoother than that on the minor axis as well. The turnover where the slope of the line vanishes marks

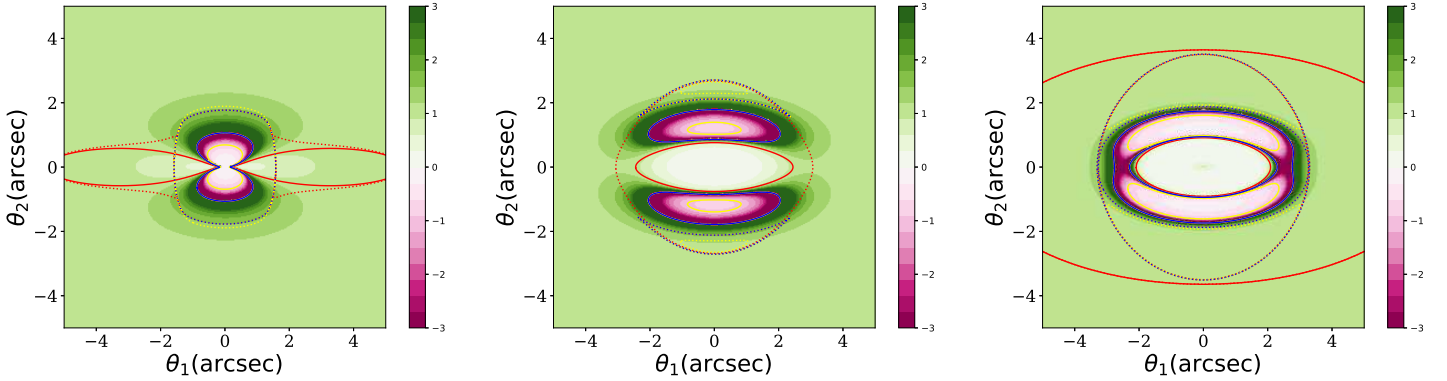


Figure 3. The two dimensional magnification map of the exponential models with lens parameters $q = 0.5$, $\theta_0 = 1.5$, $\sigma = 1.0$, and from left to right: $h = 1, 2, 3$. The green (pink) region indicates the positive (negative) magnification, and the white region indicate the demagnification region. The solid (dotted) blue line presents the critical curve (caustics) of the lens on the image (source) plane. We truncate the magnification to ± 3 for better visibility.

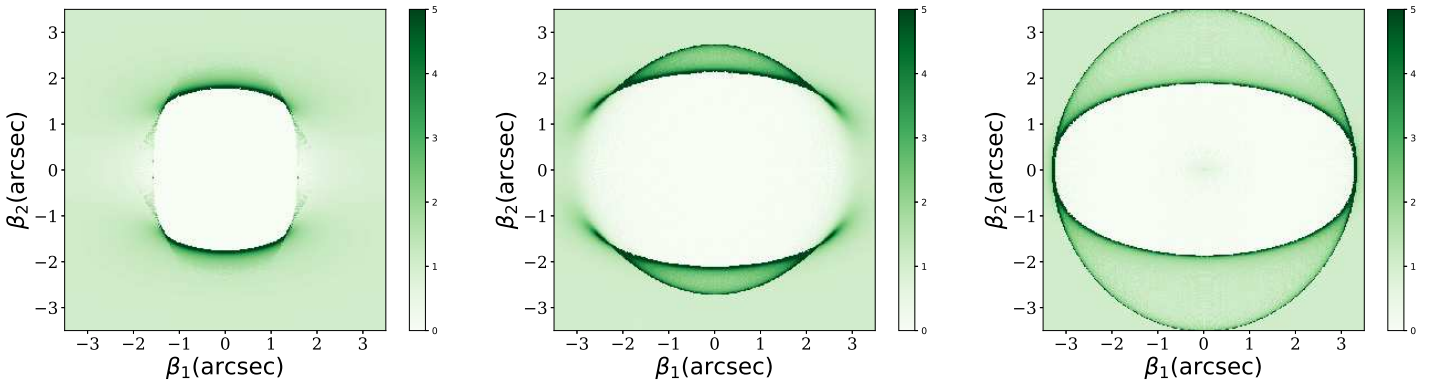


Figure 4. The magnification map of the exponential model on the source plane with the same lensing parameters as in Fig. 3. The magnification is truncated to 5 for better visibility. Notice that the coordinates have different ranges with Fig. 3.

the boundary of the exclusion region for this case. The monotonic solid lines indicate that along the major axis there is no sharp edge of the exclusion region for certain lens configurations, which can be seen from the magnification map (Fig. 8). The lens with $h = 3$ has similar properties as that of $h = 2$ and is not shown here.

The magnification maps for ESPL are shown in Fig. 8. They show distinct patterns compared with that of the exponential lenses, although the critical curves show similar shapes between the exponential lenses and the ESPL lenses. In all the ESPL lenses, the demagnification region is elongated along the major axis. Especially for the $h = 1$ lens, the criticals and magnification regions locate separately at the two sides of the major axis, while the demagnification region continues along the major axis. Also in the lenses of $h = 2, 3$, there exists weak demagnification out of the criticals along the major axis. This can also be seen from the source plane. In Fig. 9, the corresponding magnification maps of ESPL lens on source plane are present. In the left panel, the two caustics and high magnification regions are on the two sides of the major axis. Similar to the elliptical Gaussian lens, along the major axis such a lens will only cause a demagnification effect, whereas along the minor axis, the lens can cause four spikes on the light curve which is similar to the case of a circular lens. The middle panel shows a complete ellipse. The second caustic is beyond the scope of the figure. The ESPL lens of $h = 3$ has some similar properties as that of $h = 2$.

In Fig. 10, we plot the number of criticals for ESPL lenses.

The parameters q and θ_c are explored, and the same colour code is applied here as for the exponential lenses. First of all, same as that in the exponential lenses, the ellipticity increases the lensing efficiency, i.e. the core radius of sub-critical lenses grows with the decreasing of q , and the highly elongated lens even with very large core radius ($\theta_c \sim \theta_0$) can create criticals. It is also interesting to see that the singular lens, or the ESPL lens with extremely small core radius, can generate one critical curve (Fig. A3). In general, the ESPL lenses with higher power index h are more efficient in generating criticals, i.e. the area of the red region becomes smaller in the bottom panel. The shape of the critical curves generated by the lens family of $h = 3$ is similar to that of $h = 2$. We also provide a gallery of the critical curves and caustics for elliptical ESPL lenses in the appendix.

In addition, we compare the ESPL lenses between the circular model and elliptical model. In Fig. 11 we show the magnification curve along the axis of the lens. The same $\theta_0 (= 1)$ is employed for all the lenses. In the top panel, the green and black line presents the magnification curve for two SPL lenses with $\theta_c = 0.4$ and $\theta_c = 0.3$ respectively, while the red and blue line presents the curve for a ESPL lens with $\theta_c = 0.4$ and $q = 0.5$ along the minor and major axis. The SPL lens with $\theta_c = 0.4$ cannot generate critical curve (i.e. sub-critical lens), while the magnification curve along the minor axis of ESPL lens shows similar behaviour to the super-critical lens. In the bottom panel, the solid lines are identical to those in the top

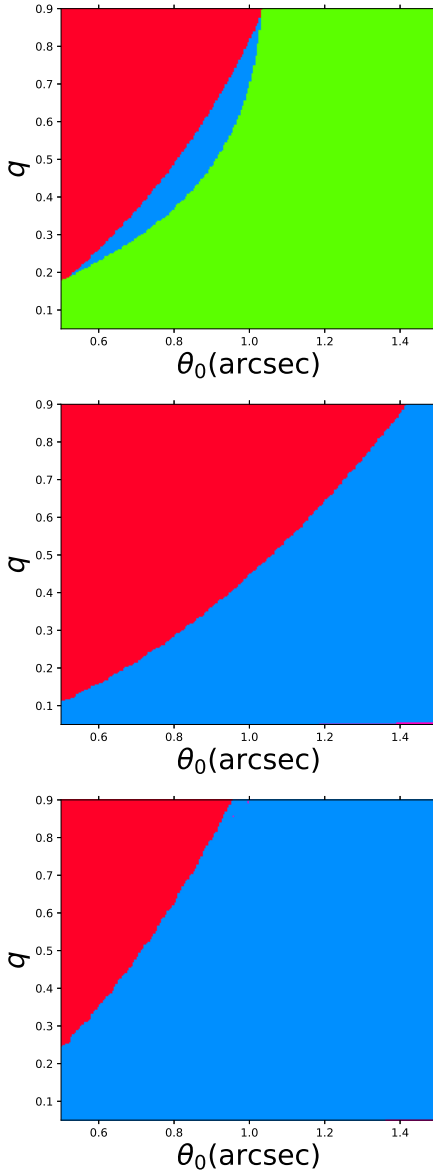


Figure 5. The figures show the number of critical curves for the elliptical exponential lens as a function of θ_0 and axis ratio q ($\sigma = 1$). From top to bottom panel, we present the case of $h = 1$, $h = 2$ and $h = 3$ families respectively. The maps are color-coded such that the number of critical curves per lens configuration is shown for 0-red, 1-green, 2-blue critical curves.

panel. Besides that we present the magnifications if we perform the observations with different wavelengths. The dotted lines present the magnifications if the wavelength in the observation is increased by 50%, while the dashed lines present that if the wavelength is decreased by 25%. In case of the shorter wavelength, both SPL and ESPL lenses become sub-critical, but the curve of SPL lens shows taming behaviour and can be distinguished from ESPL lens. Thus, the multi-bands observations can provide important constraints to the plasma lens models.

4 CONCLUSIONS

In this work, we generalize two spherical plasma lens models to produce elliptical lens models. The elliptical models are interest-

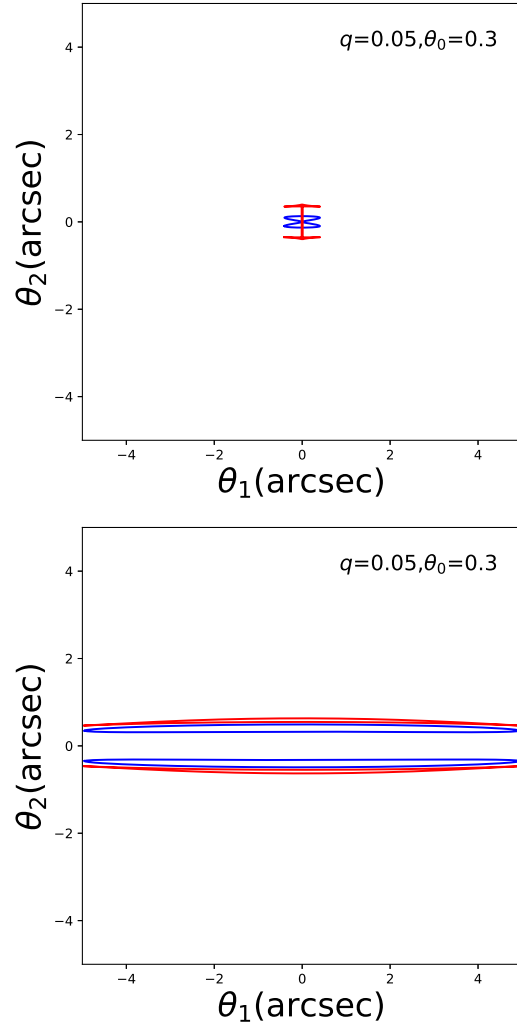


Figure 6. Two sub-critical elongated exponential lenses. The top (bottom) one show the lens of $h = 1$ ($h = 3$). The blue (red) curves are the critical curves (caustics).

ing since they represent a more general distribution for the free electrons in the ISM. Moreover, extremely elongated distributions, which are not a realistic model for the mass distribution in gravitational lenses, can be useful as plasma lenses since they provide a model for edge-on plasma sheets and filaments. We demonstrate that the details of the density profile play an important role in the lensing effect due to the density gradient and the ellipticity. We start from an elliptical plasma lensing potential, and show the analytical lensing expressions for the elliptical exponential and the softened power-law families. We performed numerical studies for each of the lens models, producing maps that catalogue the production of critical curves as a function of the lens parameters. We present these critical curve maps for each of the lensing families. We found that the ellipticity can significantly improve the lensing efficiency in generating critical curves. The elliptical lens with the sub-critical condition given by the spherical lens can also generate strong magnification variations, a marked difference from the spherical lens behaviour. This may also help in explaining the overpressure problem in the ESEs. A quantitative analysis of how strongly the ellipticity can improve the lensing efficiency with real observations is of interest. Moreover for the lens families with higher power in-

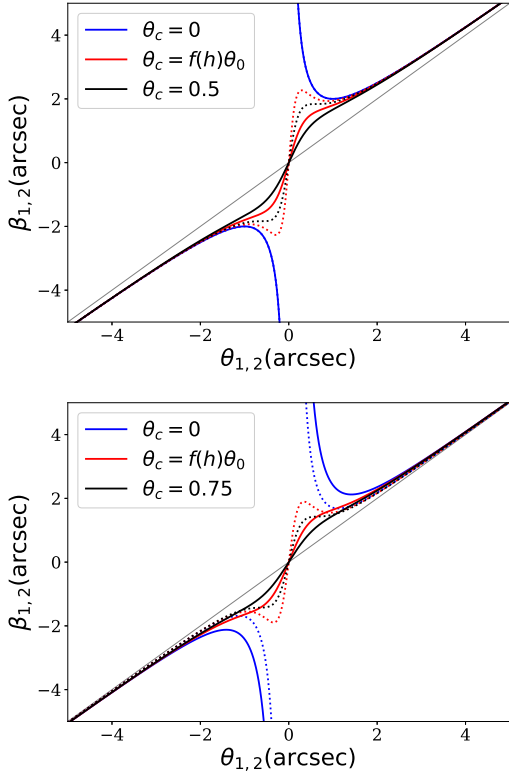


Figure 7. Young diagram of elliptical softened power law models with parameters: $\theta_0 = 1$, $q = 0.5$, $h = 1$ (top) and $h = 2$ (bottom). The solid (dotted) lines present the source positions on the major (minor) axis.

dex, the ellipticity of the lens has a larger impact in generating the critical curves.

In several cases, the lens can generate an extended demagnification region along the major axis. Along the minor axis, the magnification curve shows a behaviour similar to that of the circular lens.

The elliptical lenses offer a rich variety of magnifications for background sources. Therefore, model degeneracy may exist in fitting one dimensional light curves. In addition, our study only considers a single frequency. Radio observations contain multi-frequency power spectra. The magnification of plasma lensing strongly depends on the observing frequency ($\mu \sim \lambda^4$). Thus, the magnification curve over a frequency band may show dramatic changes, especially at the critical points. Therefore, the multi-frequency light curve of the background source should be used in plasma lensing modelling and can provide tight constraints on the lens parameters and even break the model degeneracy altogether. In addition, wide frequency observations are also useful for constraining pulsar secondary spectra as discussed by Kerr et al. (2018).

Our work opens several other questions for future work, especially in terms of the highly asymmetrical distributions. Besides the ellipticity, the arc-shape or the small scale variations, i.e. clumpiness will also introduce a large variety of magnification and image properties. In addition, the elliptical lenses require further study and comparison with real ESE observations, a topic we plan to explore in future work. Polarization can also provide a wealth of information on both the lens itself as well as the magnetic field along the line of sight. Detailed studies on the polarization pattern will also be useful and interesting.

APPENDIX A: A GALLERY OF CRITICAL CURVES AND CAUSTICS

In the appendix, we present the critical curves and caustics for the elliptical models in this work. We have tried to display critical curves and caustics from each region shown in Fig. 5 and 10. Some of the caustics extend beyond the scope of the panel. We omit those large caustics in order to present better resolution of the inner region.

A1 Elliptical exponential lenses

We show the critical curves (blue) and caustics (red) for the elliptical exponential lenses with $h = 1, 2$ in Fig. A1 and A2 respectively. We calculate the critical curves by increasing the axis ratio from 0.05 to 0.75. The left and middle panel in the magnification map (Fig. 3) correspond to the bottom left in Fig. A1 and top middle panel in Fig. A2. For $h = 1$, the dual-arrow shape curves evolve into an elliptical shape as the axis ratio increases. In most cases, the lenses with $h = 1$ can generate one critical curve, while the Gaussian models ($h = 2$) can generate two. The bottom right panel of Fig. A1 present the transitional case of two criticals. In Fig. A2, for sufficiently large θ_0 , the two leaf-shaped curves on the two sides of the major axis will merge to two ellipses as the axis ratio increases. The inner critical curve maps to the outer caustics, and the major axis of the outer caustics aligns with the minor axis of the lens. Moreover, the two leaves generated by the Gaussian model (top middle panel) show similarity with that of the dual-component Gaussian lens model, which may also cause model degeneracy. The critical curves of lenses with $h = 3$ show similar behaviours as with $h = 2$, and for brevity we do not present them here.

A2 Softened power-law lenses

In this section, we show examples of criticals and caustics of the elliptical ESPL lenses. Firstly, Fig. A3 presents the singular lens evolving from an elongated shape to a circular shape. The singular lens can only generate one critical even for highly elongated cases. For the lens of $h = 1$, the critical curve crosses the two axes at the same length ($\theta_1 = \theta_2 = \theta_0$) for all q , while this is not the case of the lenses of $h = 2, 3$. Moreover, from the three panels of $q = 0.5$, one can see that the elliptical shape becomes more significant with large value of h .

In Figs. A4 and A5, we present the critical curves and caustics for the ESPL lens of index $h = 1$ and $h = 2$ respectively. The top and middle panel in the magnification map (Fig. 8) correspond to the bottom middle panel in Fig. A4 and A5. The core radius causes complex behaviour, i.e. the emergence of the second inner critical curve in the core region of the lens. Increasing the core radius θ_c will cause the merger of the inner and outer critical, and forming two separated curves on both sides of the major axis.

ACKNOWLEDGMENTS

We thank the referee for constructive and valuable comments which increase the scope of our work significantly and improve the overall quality even in some details of our paper. We thank Artem Tuntsov, Oleg Yu. Tsupko and Shude Mao for interesting discussions. XE is supported by NSFC Grant No. 11473032 and No. 11873006. AR wishes to acknowledge the contribution of the Brandon University Research Committee.

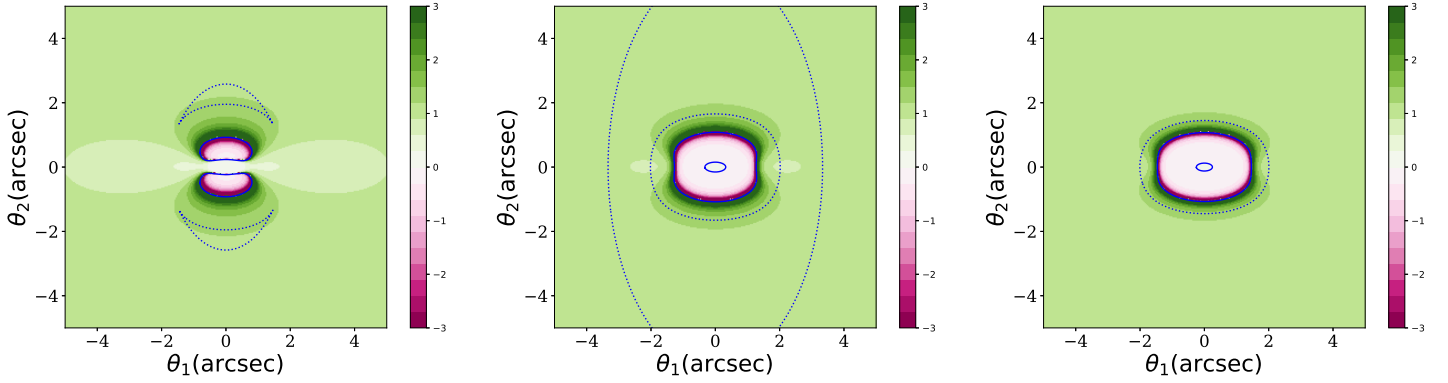


Figure 8. The two dimensional magnification map of softened power-law lens with parameters $\theta_0 = 1$, $q = 0.5$, $\theta_c = 0.3$, $h = 1$ (left), $h = 2$ (middle) and $h = 3$ (right). The same color code is applied as in Fig. 3.

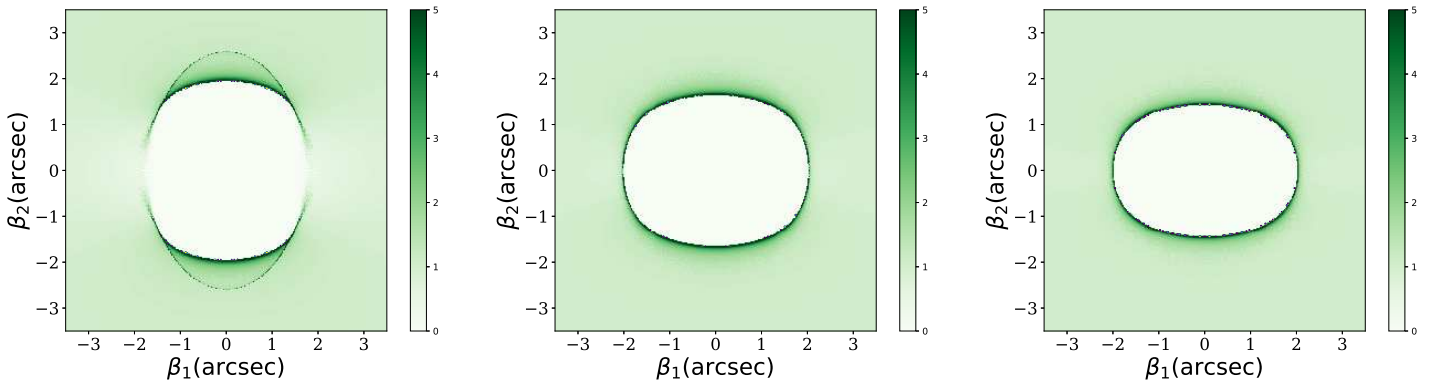


Figure 9. The magnification map of the ESPL model on the source plane with the same parameters as in Fig. 8. The magnification is truncated at 5, and the maps are slightly zoomed into the center region for better visibility.

REFERENCES

- Allgood B., Flores R. A., Primack J. R., Kravtsov A. V., Wechsler R. H., Faltenbacher A., Bullock J. S., 2006, *MNRAS*, **367**, 1781
- Bannister K. W., Stevens J., Tuntsov A. V., Walker M. A., Johnston S., Reynolds C., Bignall H., 2016, *Science*, **351**, 354
- Barnabè M., et al., 2012, *MNRAS*, **423**, 1073
- Binney J., Tremaine S., 1987, *Galactic dynamics*, Princeton University Press, Princeton, NJ
- Bisnovatyi-Kogan G. S., Tsupko O. Y., 2009, *Gravitation and Cosmology*, **15**, 20
- Blandford R. D., Kochanek C. S., 1987, *ApJ*, **321**, 658
- Brisken W. F., Macquart J. P., Gao J. J., Rickett B. J., Coles W. A., Deller A. T., Tingay S. J., West C. J., 2010, *ApJ*, **708**, 232
- Clegg A. W., Fey A. L., Lazio T. J. W., 1998, *ApJ*, **496**, 253
- Clowe D., Bradač M., Gonzalez A. H., Markevitch M., Randall S. W., Jones C., Zaritsky D., 2006, *ApJ*, **648**, L109
- Coles W. A., et al., 2015, *ApJ*, **808**, 113
- Cordes J. M., Chatterjee S., 2019, arXiv:1906.05878, p. arXiv:1906.05878
- Cordes J. M., Lazio T. J. W., 2002, ArXiv: 0207156,
- Cordes J. M., Rickett B. J., Stinebring D. R., Coles W. A., 2006, *ApJ*, **637**, 346
- Cordes J. M., Wasserman I., Hessels J. W. T., Lazio T. J. W., Chatterjee S., Wharton R. S., 2017, *ApJ*, **842**, 35
- Czoske O., Barnabè M., Koopmans L. V. E., Treu T., Bolton A. S., 2012, *MNRAS*, **419**, 656
- Dong L., Petropoulou M., Giannios D., 2018, *MNRAS*, **481**, 2685
- Er X., Rogers A., 2018, *MNRAS*, **475**, 867
- Fiedler R. L., Dennison B., Johnston K. J., Hewish A., 1987, *Nature*, **326**, 675
- Goldreich P., Sridhar S., 2006, *ApJ*, **640**, L159
- Grillo G., Cordes J., 2018, preprint, (arXiv:1810.09058)
- Hill A. S., Joung M. R., Mac Low M.-M., Benjamin R. A., Haffner L. M., Klingenberg C., Waagan K., 2012, *ApJ*, **750**, 104
- Kassiola A., Kovner I., 1993, *ApJ*, **417**, 450
- Keeton C. R., 2001, ArXiv:0102341,
- Keeton C. R., Kochanek C. S., 1998, *ApJ*, **495**, 157
- Kerr M., Coles W. A., Ward C. A., Johnston S., Tuntsov A. V., Shannon R. M., 2018, *MNRAS*, **474**, 10
- Koopmans L. V. E., et al., 2009, *ApJ*, **703**, L51
- Kormann R., Schneider P., Bartelmann M., 1994, *A&A*, **284**, 285
- Li D., Lin F. X., Main R., Pen U.-L., van Kerkwijk M. H., Yang I., 2018, ArXiv:1809.10812,
- Li R., et al., 2019, arXiv e-prints, p. arXiv:1903.09282
- Lorimer D. R., Bailes M., McLaughlin M. A., Narkevic D. J., Crawford F., 2007, *Science*, **318**, 777
- Mao S., 2012, *Research in Astronomy and Astrophysics*, **12**, 947
- Muhleman D. O., Johnston I. D., 1966, *Physical Review Letters*, **17**, 455
- Nakamura T., Deguchi S., 1999, *Progress of Theoretical Physics Supplement*, **133**, 137
- Nambu Y., 2013, *International Journal of Astronomy and Astrophysics*, **3**, 1
- Narayan R., Bartelmann M., 1996, ArXiv Astrophysics e-prints,
- Navarro J. F., Frenk C. S., White S. D. M., 1997, *ApJ*, **490**, 493
- Pen U.-L., 2018, *Nature Astronomy*, **2**, 842
- Pen U.-L., Levin Y., 2014, *MNRAS*, **442**, 3338
- Perlick V., 2000, *Ray Optics, Fermat's Principle, and Applications to Gen-*

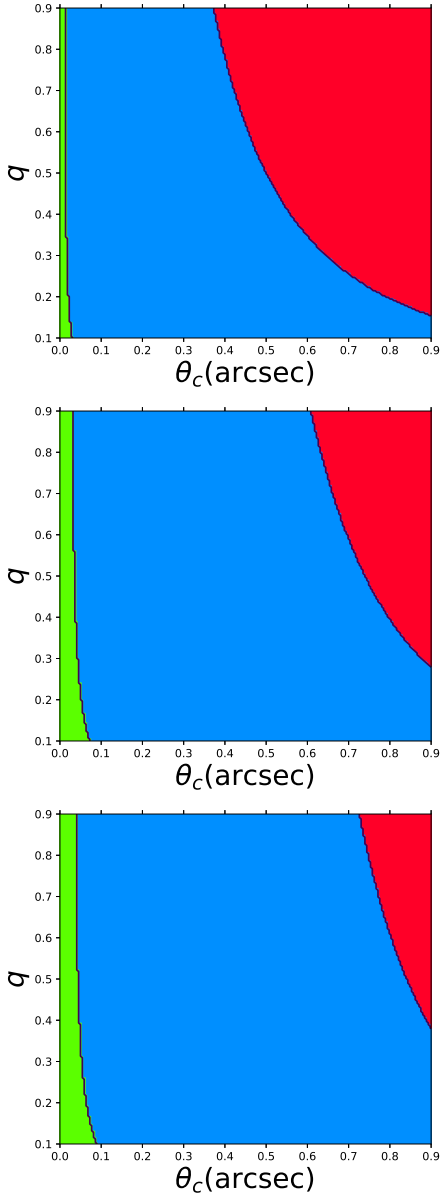


Figure 10. This figure shows the number of critical curves for the elliptical ESPL lenses as a function of angular core radius θ_c and axis ratio q ($\theta_0 = 1$). The same color code as Fig. 5 is used in this figure. From top to bottom, the lens families of $h = 1, 2, 3$ are present.

eral Relativity. Springer-Verlag
 Rogers A., 2017, *MNRAS*, **465**, 2151
 Rogers A., Er X., 2019, *MNRAS*, **485**, 5800
 Romani R. W., Blandford R. D., Cordes J. M., 1987, *Nature*, **328**, 324
 Scalo J., Elmegreen B. G., 2004, *ARA&A*, **42**, 275
 Schaller M., et al., 2015, *MNRAS*, **451**, 1247
 Schneider P., Ehlers J., Falco E. E., 1992, *Gravitational Lenses*, doi:10.1007/978-3-662-03758-4.
 Schrabback T., et al., 2010, *A&A*, **516**, A63
 Schrabback T., et al., 2015, *MNRAS*, **454**, 1432
 Schramm T., 1990, *A&A*, **231**, 19
 Shannon R. M., Cordes J. M., 2017, *MNRAS*, **464**, 2075
 Simard D., Pen U.-L., 2018, *MNRAS*,
 Stinebring D., 2007, in Haverkorn M., Goss W. M., eds, *Astronomical Society of the Pacific Conference Series Vol. 365, SINS - Small Ionized and Neutral Structures in the Diffuse Interstellar Medium*. p. 254

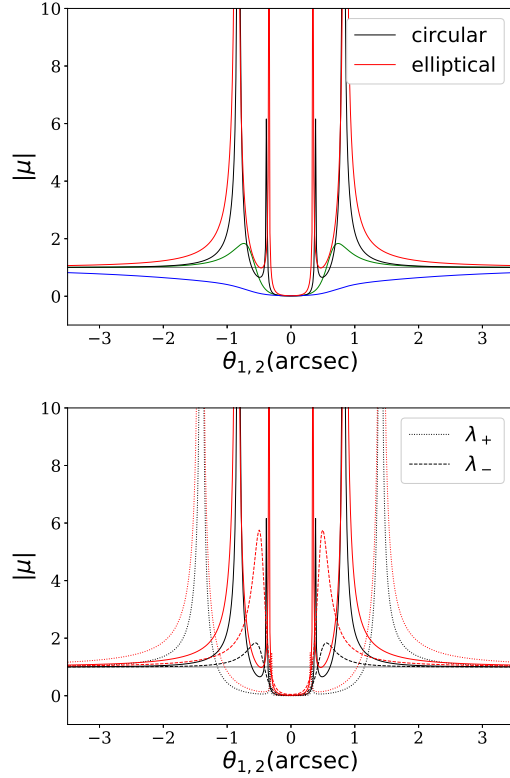


Figure 11. Comparison of magnification curves between circular ($q = 1$) and elliptical ($q = 0.5$) lens for a softened power law model with parameters: $h = 1$. In the top panel, we use $\theta_0 = 1$ for all the lens models. The green (black) line presents the curve of SPL lens with $\theta_c = 0.4(0.3)$. The red (blue) line presents the curve of ESPL lens along the minor (major) axis. In the bottom panel, the solid red and black lines are identical to that in the top panel. The dashed (dotted) lines present the curves for same lens parameter but with shorter the wavelength $\lambda_- = 0.75\lambda$ (longer the wavelength $\lambda_+ = 1.5\lambda$) in the observation.

Stinebring D. R., McLaughlin M. A., Cordes J. M., Becker K. M., Goodman J. E. E., Kramer M. A., Shekard J. L., Smith C. T., 2001, *ApJ*, **549**, L97
 Suresh A., Cordes J. M., 2018, ArXiv:1808.09471,
 Tessore N., Metcalf R. B., 2015, *A&A*, **580**, A79
 Tuntsov A. V., Walker M. A., Koopmans L. V. E., Bannister K. W., Stevens J., Johnston S., Reynolds C., Bignall H. E., 2016, *ApJ*, **817**, 176
 Tuntsov A. V., Stevens J., Bannister K. W., Bignall H., Johnston S., Reynolds C., Walker M. A., 2017, *MNRAS*, **469**, 5023
 Vedantham H. K., et al., 2017a, *ApJ*, **845**, 90
 Vedantham H. K., et al., 2017b, *ApJ*, **845**, 90
 Walker M. A., Melrose D. B., Stinebring D. R., Zhang C. M., 2004, *MNRAS*, **354**, 43
 Xu D., Sluse D., Schneider P., Springel V., Vogelsberger M., Nelson D., Hernquist L., 2016, *MNRAS*, **456**, 739

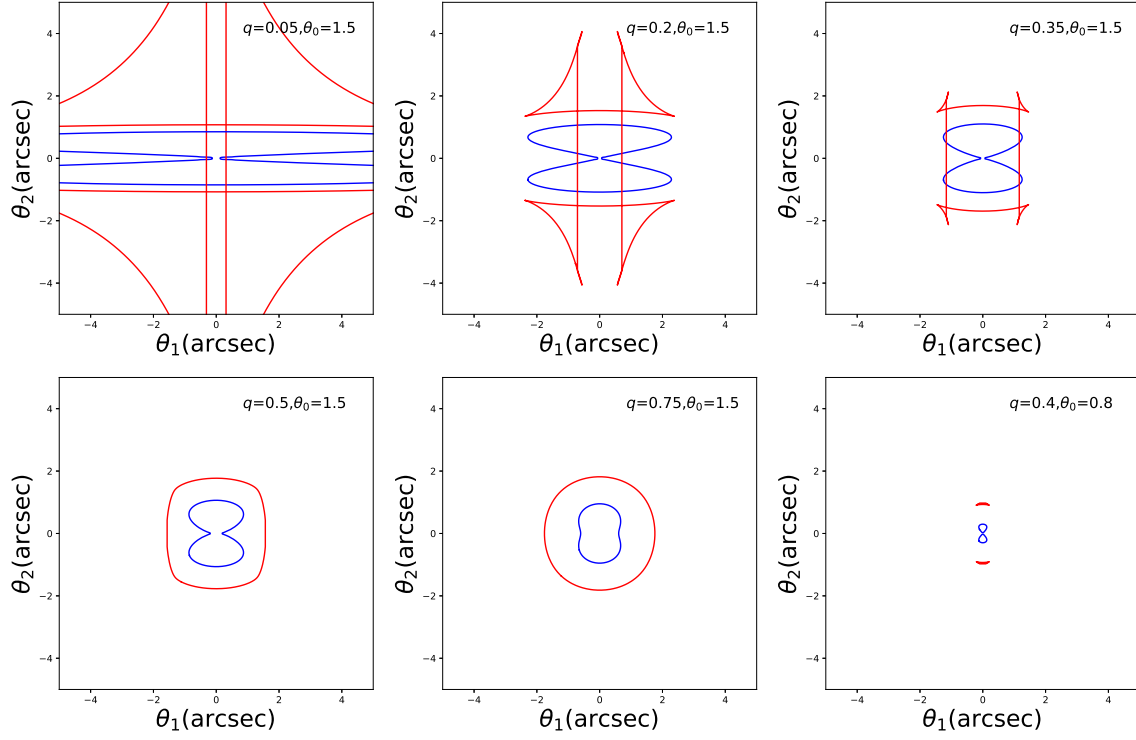


Figure A1. The critical curves (blue) and caustics (red) of the elliptical exponential lens with $h = 1$ and $\sigma = 1$. The axis ratio and the characteristic radius are given at the top right corner in each panel.

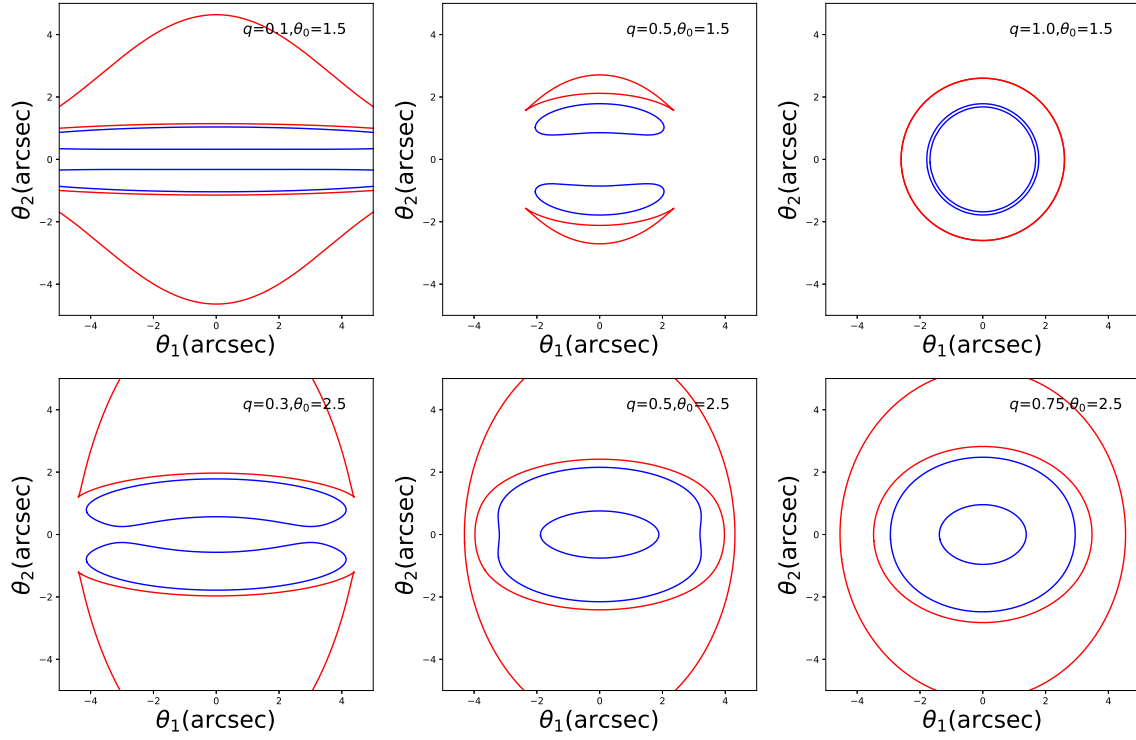


Figure A2. The critical curves (blue) and caustics (red) of the elliptical exponential lens with $h = 2$ and $\sigma = 1$.

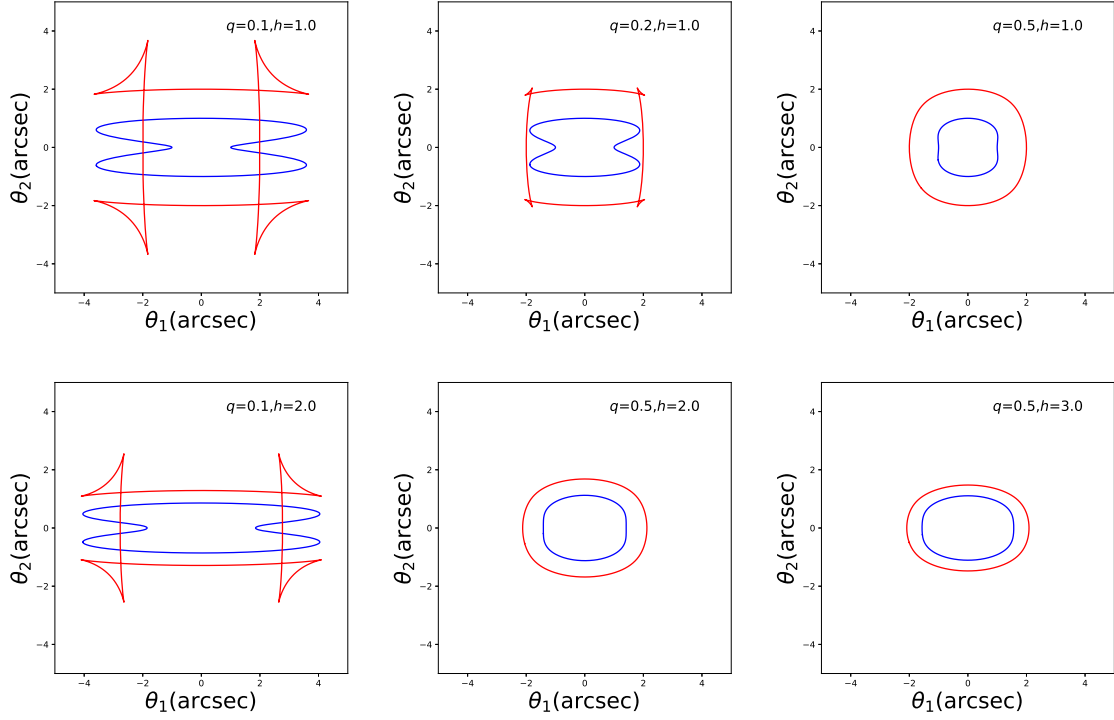


Figure A3. The critical curves (blue) and caustics (red) of the elliptical singular power-law lenses ($\theta_c = 0$) with $\theta_0 = 1$ arcsec. The power index and axis ratio are given at top corner of each panel.

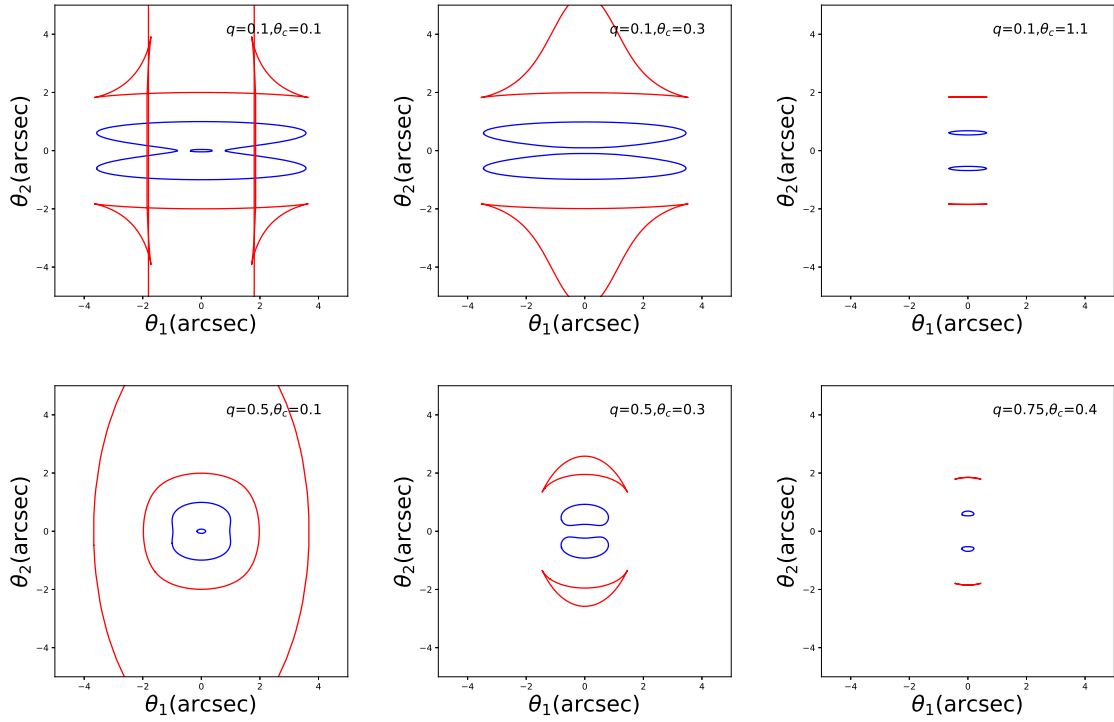


Figure A4. The critical curves (blue) and the caustics (red) of the ESPL lens with parameters: $\theta_0 = 1$ arcsec and $h = 1$. The core radius and the axis ratio are given at the top right corner of each panel.

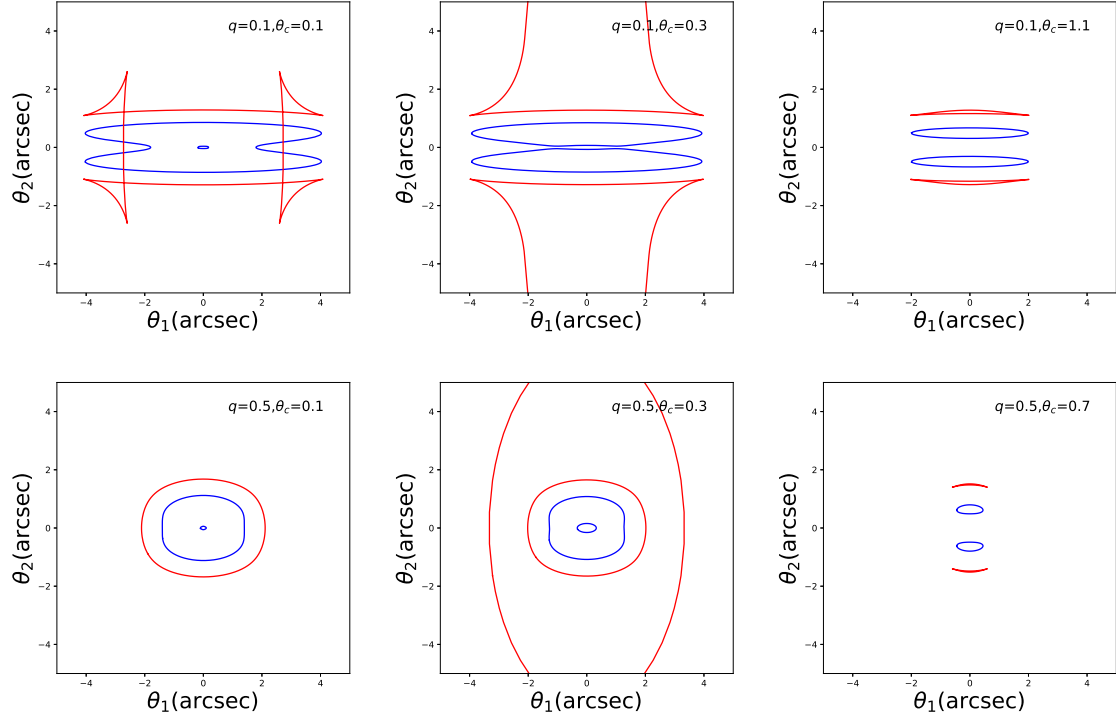


Figure A5. Same as Fig. A4 with $h = 2$.